Static Hybrid Quantum Nodes: Toward Perfect State Transfer on a Photonic Chip

Zhaohua Tian,[1,2] Pu Zhang,[1,2,*] and Xue-Wen Chen[1,2,†]

[1]*School of Physics and Wuhan National Laboratory for Optoelectronics, Huazhong University of Science and Technology, Luoyu Road 1037, Wuhan 430074, People's Republic of China*

[2]*Institute for Quantum Science and Engineering, Huazhong University of Science and Technology, Luoyu Road 1037, Wuhan 430074, People's Republic of China*

Hybrid integrated quantum photonic circuits have the potential to scale up the number of quantum nodes and to build a network with distributed quantum-information-processing units at affordable resources. A central need of such systems is to have near-unity success-rate state transfer between the quantum nodes. This turns out to be a grand challenge since stringent conditions of spatial mode matching and time-reversal symmetry between the sending and receiving nodes have to be simultaneously satisfied. Here we devise a type of hybrid quantum node consisting of a single solid-state quantum system and a coupled-cavity structure toward achieving perfect state transfer between two distant nodes connected via waveguides. The hybrid node possesses flexibility in tailoring the temporal profile of the emitted single-photon wave packet without any dynamic modulation. In particular, we show it could emit time-reversal symmetric single-photon wave packets and fully couple the emission to the waveguide, fulfilling the conditions for perfect quantum state transfer. We develop a complete theoretical framework and provide a clear physical picture of the protocol for transferring a superposition state. We show ideally the simple node structures with one, two, and three chain-coupled microring resonators could lead to total success rates of 90.5%, 97.5%, and 99.3%, respectively. We then further discuss the influence of imperfections and experimental realizations of our scheme with integrated quantum photonics.

I. INTRODUCTION

For emerging quantum technologies, scaling up cooperatively the number of quantum nodes in a system is crucial and difficult. One viable solution is hybrid integrated quantum photonics, where a large number of quantum nodes and optical components could be integrated on one chip [1–4]. Indeed, nanofabricated resonators, waveguides and beam splitters on one chip can have excellent system stability and provide fine control over photon behavior as well as the coupling with the quantum systems [3,5–10]. In a hybrid quantum photonic circuit, single solid-state quantum systems could communicate via single photons through waveguides and thus promise an on-chip network with distributed quantum-information-processing units [11,12]. A central need of this scenario is to have both high-efficiency and high-fidelity quantum state transfer between the nodes, which means that an emitted single photon carrying the state information from the sending node should be fully directed to the receiving node for perfect absorption. This requires not only spatial mode matching between the emission and absorption but also

an on-chip time-reversal operation on the emitted exponentially decaying single-photon wave packet [13–16], which is a great challenge. To invert an optical pulse, researchers have recently considered using dynamically modulated cavity arrays [17,18] and direct modulation with an acousto-optic modulator [16]. Despite impressive progress, inverting a single-photon wave packet (typically of nanoseconds' duration) for each node on the chip without loss remains difficult and becomes formidably expensive as the size of the system increases.

In a broader perspective, quantum state transfer is highly relevant for the implementations of quantum-communication protocols and distributed quantum computation, and has been studied for decades. Various approaches based on dynamic single-photon wave-packet shaping, dynamic modulation of the cavity and matter systems, and adiabatic passage have been proposed for high-fidelity and success-rate state transfer through free space or optical fiber [19–24]. A milestone experiment by Ritter *et al.* [25] implemented the dynamic wave-packet shaping protocol [19], and achieved a fidelity of 84% and an overall success rate of 0.2% for the whole state-transfer process between two single trapped atoms. Towards the goal with both high fidelity and efficiency, there are also experimental reports on state swap between a quantum

*puzhang0702@hust.edu.cn
†xuewen_chen@hust.edu.cn

node and a photon [26–28], and single-photon wave-packet shaping based on four-wave mixing processes of a cold atomic ensemble [29–31]. Nevertheless, existing schemes generally need delicate dynamic control of the quantum systems or/and specific atomic level schemes, being intrinsically incompatible with solid-state integration. The realization of large-scale quantum networks on a photonic chip remains elusive.

Here we propose a class of quantum nodes consisting of a single solid-state quantum system and a coupled-cavity structure to circumvent the challenges without dynamic modulation. The hybrid quantum node offers extra degrees of freedom to synthesize a time-reversal symmetric single-photon wave packet for the node emission via the interference of the eigenstates of the hybrid system. In addition, by interfacing the node with a waveguide, all the emission of the node can be funneled into the single waveguide mode and delivered towards the receiving node, making the emission and absorption spatially mode matched. We develop a general theoretical framework for the protocol and paint a clear physical picture of the state transfer. We show theoretically with a series of simple configurations based on microring resonators that it is possible to achieve quantum state transfer between two distant nodes with near-unity overall success rate. Moreover, we discuss the effects of imperfections and possible experimental realizations.

II. HYBRID QUANTUM NODE AND THEORETICAL FORMULATION

The goal is to transfer a quantum state or one excitation registered in the emitter of the sending node with ideally unity fidelity and efficiency to the emitter of the receiving node through a single-photon wave packet in the waveguide. This goal can be achieved when the emission of the sending node couples with unity efficiency to the waveguide and simultaneously the emitted single-photon wave packet possesses a time-reversal symmetry [14,15]. The first condition could be satisfied by using photonic crystal waveguides [2], plasmonic nanowires [32], or dielectric-wire interfaced plasmonic nanocone structures [33]. However, the resulting single-photon emission has an exponentially decaying temporal profile because the emitter couples irreversibly to a continuum of waveguide modes with an infinite number of degrees of freedom. To get around this difficulty, we introduce a type of hybrid quantum node consisting of a matter quantum system or two-level system (TLS) and a cavity cluster, which allows the TLS to couple to a finite number of degrees of freedom [34]. The hybrid node is then interfaced with the waveguide and couples to the continuum. The hybrid node enables flexible control over the amplitude, phase, and complex eigenfrequency of each eigenstate of the coupled
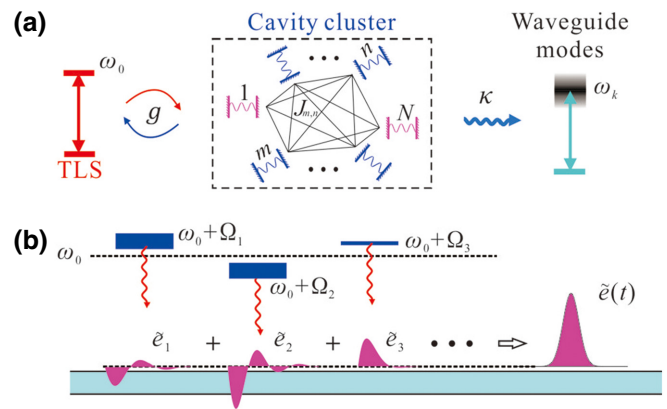

FIG. 1. Structure and physics of the proposed hybrid quantum node. (a) Schematic diagram of the node and coupling scheme; (b) the eigenstates of the node with eigenvalues Ω_n and single-photon wave-packet synthesis via the interference of the eigenstates of the hybrid system.

system, which can be harnessed for static single-photon wave-packet shaping.

Figure 1(a) schematically illustrates the proposed composite quantum node and its coupling schemes. The N cavities in the cluster form a nontrivial connection topology represented by the coupling rate matrix **J**. The cavity cluster interfaces with the TLS and the waveguide with the first and Nth cavity, respectively. We assume that the original spontaneous decay rate of the TLS Γ_0 is much smaller than its coupling with the cavity and the radiation decay rates of the cavities Γ_C are negligible compared to the intercavity and cavity-waveguide coupling rates. These conditions guarantee predominant emission of the TLS eventually funnels into the waveguide. The assumptions are realistic with the consideration of developments of integrated photonics and solid-state quantum technologies in recent decades [2,35–37]. The composite quantum node can be characterized in terms of the eigenstates of the entire coupled system. Consequently, the time evolution of the single-photon probability amplitude in the Nth cavity coupled to the waveguide continuum can be considered as a superposition of the decays from all individual eigenstates, as schematically depicted in Fig. 1(b). Crucially, the probability amplitude in the waveguide is a copy of that in the Nth cavity because the cavity couples to the waveguide continuum with an infinite number of degrees of freedom. Therefore, the single-photon pulse amplitude in the waveguide can be synthesized to a desired shape by controlling the amplitudes and relative phases of the eigenstates of the cavity cluster. In other words, the cavity cluster thus provides flexible controls, including TLS-cavity coupling constant g, intercavity coupling rates $J_{m,n}$, and cavity-waveguide coupling rate κ, towards the synthesis of a time-reversal symmetric single-photon wave packet.

The emission and excitation processes of the quantum node can be rigorously formulated by applying the waveguide-cavity quantum electrodynamic model under the following system Hamiltonian [6,9,38]:

$$\hat{H} = \hat{H}_0 + \hat{H}_{AC} + \hat{H}_{CC} + \hat{H}_{CW}. \tag{1}$$

It consists of the uncoupled Hamiltonian $\hat{H}_0/\hbar = (\omega_0 - i\Gamma_0/2)\hat{\sigma}_+\hat{\sigma}_- + \sum_{n=1}^N(\omega_n - i\Gamma_C/2)\hat{a}_n^\dagger\hat{a}_n + \sum_k \omega_k\hat{c}_k^\dagger\hat{c}_k$, the TLS-cavity coupling $\hat{H}_{AC}/\hbar = g(\hat{\sigma}_+\hat{a}_1 + \text{H.c.})$ with g being the coupling constant, the intercavity coupling $\hat{H}_{CC}/\hbar = \sum_{m=1}^N \sum_{n=1,n\neq m}^N J_{m,n}(\hat{a}_m^\dagger\hat{a}_n + \text{H.c.})$ with $J_{m,n}$ being the mutual coupling rate, and the cavity-waveguide coupling $\hat{H}_{CW}/\hbar = \sum_k(V_k\hat{a}_N^\dagger\hat{c}_k + \text{H.c.})$ with V_k being the coupling rate. Here ω_0 is the TLS transition frequency with Γ_0 being the spontaneous decay rate. $\hat{\sigma}_\pm$ is the raising or lowering operator. The cavities are described by the photon creation (annihilation) operators $\hat{a}_n^\dagger$ ($\hat{a}_n$), the resonant frequencies ω_n and the decay rate Γ_C. Usual rotating-wave approximation is applied. The waveguide continuum is denoted by the wave vector k, frequency ω_k, and the corresponding creation (annihilation) operator $\hat{c}_k^\dagger$ ($\hat{c}_k$). For state transfer the system is limited to the one-excitation sector and each node can be described in the interaction picture by

$$|\psi\rangle = \left[c_0(t)\hat{\sigma}_+ + \sum_{n=1}^N c_n(t)\hat{a}_n^\dagger + \sum_k c_k(t)\hat{c}_k^\dagger \right]|\varnothing\rangle, \tag{2}$$

where $|\varnothing\rangle$ denotes the zero-excitation state. The time evolution of the probability amplitudes c_0, c_n, and c_k can be determined by substituting Eq. (2) into the Schrödinger equation $i\hbar\partial_t|\psi\rangle = \hat{\mathscr{V}}|\psi\rangle$, where $\hat{\mathscr{V}}$ is the interaction Hamiltonian. Eliminating the continuum (see Appendix A), we obtain a dynamic equation for the probability amplitude vector $\mathbf{c} = [c_0, c_1, \ldots, c_N]^T$ as

$$\partial_t\mathbf{c} = -i\mathbf{H}\mathbf{c} + \mathbf{d}. \tag{3}$$

The Hamiltonian is expressed herein as a matrix $\mathbf{H} = [-i\Gamma_0/2, \mathbf{g}; \mathbf{g}^T, \mathbf{H}_R]$ with $\mathbf{g} = [g, 0, \ldots, 0]$ and $\mathbf{H}_R = \text{diag}(\delta_1, \delta_2, \ldots, \delta_N - i\kappa/2) - i\Gamma_C\mathbf{I}/2 + \mathbf{J}$. $\delta_n = \omega_n - \omega_0$ are the detunings of the cavity resonances with respect to the TLS transition and κ is the cavity-waveguide coupling rate. The inhomogeneous term $\mathbf{d}$ serves as the drive for the system. The probability amplitude $e(t)$ of the emitted single photon in the waveguide is directly related to $c_N(t)$ as $e(t) = -i\sqrt{\kappa}c_N(t)$ (see Appendix A).

Next we describe the protocol of quantum state transfer between two identical nodes ($A \rightarrow B$). While the principle can be fully explained with two TLSs, practical implementation at optical frequencies may need two three-level Λ systems. Thus we consider the quantum information

is encoded in the two lower-lying states ($|g_0\rangle$, $|g_1\rangle$) of a three-level Λ system, where the transition from $|g_0\rangle$ to the excited state $|e\rangle$ is coupled to the cavity. Initially node A is in a superposition state $p_0|g_{0A}\rangle + p_1|g_{1A}\rangle$ and node B is prepared in the state $|g_{0B}\rangle$. The deterministic state transfer gets started by coherently bringing the occupation at $|g_{1A}\rangle$ to $|e_A\rangle$ with a proper π pulse [39]. The system now can be compactly expressed with the product state $(p_1\hat{\sigma}_+^A + p_0)|g_{0A}, 0, g_{0B}\rangle$, where $|0\rangle$ represents no photon in the waveguide. With the emission of a single photon from node A into the waveguide, the system state evolves to $p_1|g_{0A}, 1, g_{0B}\rangle + p_0|g_{0A}, 0, g_{0B}\rangle$. Upon propagating to the receiving node, the emitter is excited to $|e_B\rangle$ with the resulting state $(p_1'\hat{\sigma}_+^B + p_0)|g_{0A}, 0, g_{0B}\rangle$. Then the receiving process is terminated at an optimal time t_f by coherently bringing $|e_B\rangle$ to $|g_{1B}\rangle$ with another π pulse. This completes the transfer process with node B in the superposition state $p_0|g_{0B}\rangle + p_1'|g_{1B}\rangle$. If the single-photon wave packet possesses time-reversal symmetry and experiences no loss, the superposition state can be perfectly recovered ($p_1' = p_1$). We note t_f can be determined from theoretical design and postfabrication calibration. Precise timing (<1 ps) for switching off is possible with a clock distribution network [40].

We now discuss the emission process with $\mathbf{d} = 0$ and the initial condition of $\mathbf{c}(0) = [p_1, 0, \ldots, 0]^T$. Equation (3) admits a formal solution of $\mathbf{c}(t) = e^{-i\mathbf{H}t}\mathbf{c}(0)$ and the emitted pulse amplitude takes the form of

$$e(t) = p_1 \sum_{n=1}^{N+1} \alpha_n e^{-i\Omega_n t} \equiv p_1\tilde{e}(t). \tag{4}$$

Here Ω_n is the nth complex eigenvalue of $\mathbf{H}$ and in general the complex amplitude α_n is determined numerically. One clearly sees from Eq. (4) that the node has $N + 1$ eigenstates and the pulse shape is a result of superposition of all the states, confirming the physical picture of interference (superposition). By defining $e_n(t) = \alpha_n e^{-i\Omega_n t}$, one sees that the pulse profile can be shaped by tuning the complex amplitudes and eigenvalues as schematically shown in Fig. 1(b). While the real part of Ω_n indicates the energy shift relative to ω_0, the imaginary part means an exponential decay of the eigenstate due to coupling to the waveguide as well as various channels of loss. Thus, by tuning the normalized coupling parameters $(J_{m,n}, \kappa)/g$, it is possible to generate time-reversal symmetric single-photon wave packets. To quantify the pulse symmetry, we introduce a symmetry factor

$$\beta = \max_{t_0}\left(\left|\int_{-\infty}^{\infty} \tilde{e}(t)\tilde{e}(2t_0 - t)dt\right|^2\right), \tag{5}$$

with $\beta = 1$ denoting a perfectly symmetric pulse. From Eq. (3) and the expression of $\mathbf{H}$, one sees that only the
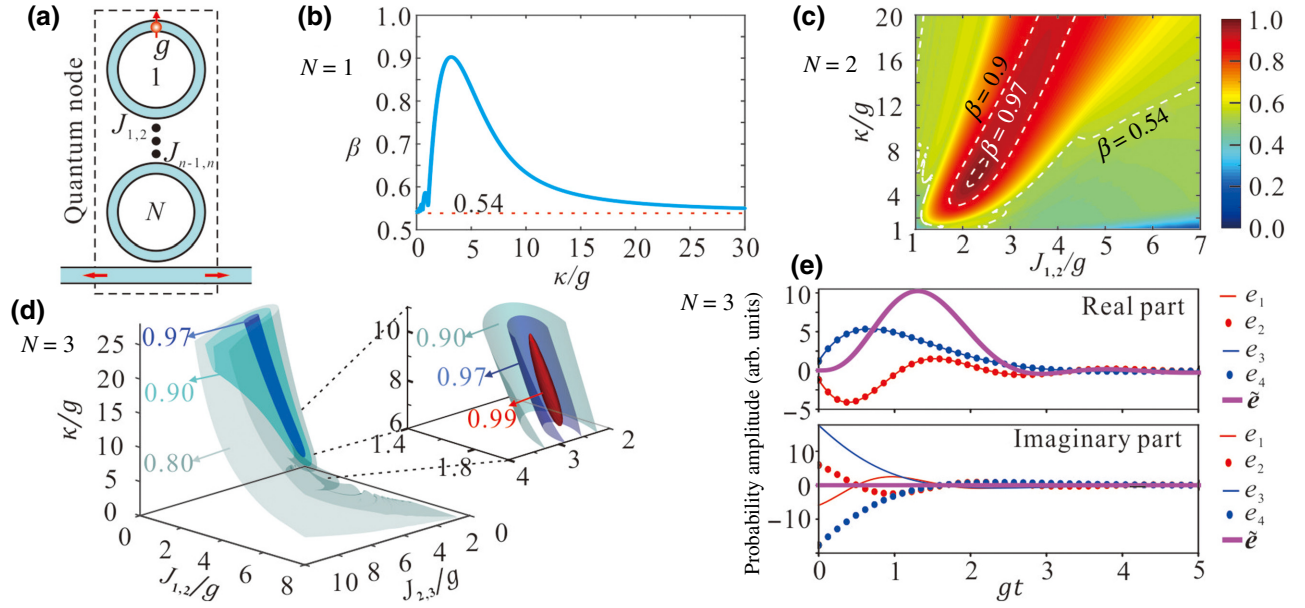
FIG. 2. Microring-resonator-chain-based hybrid quantum node and single-photon wave-packet synthesis. (a) The schematic diagram of the node; (b)–(d) wave-packet symmetric factor β as functions of κ/g, $(J_{12}, \kappa)/g$, and $(J_{12}, J_{23}, \kappa)/g$ for $N = 1 \sim 3$; (e) the optimal normalized pulse shape $\tilde{e}(t)$ for $N = 3$ is shown as a coherent superposition of emissions from eigenstates.

ratios, i.e., $(J_{m,n}, \kappa)/g$, affect the pulse shape. Although arbitrary connection topologies seem to lend additional design freedom, a full coupling matrix **J** in fact contains more elements than necessary for taming the pulse shape. In the following, the specific topology of the cavity chain in Fig. 2(a) is elaborated as it is facile to realize and proves adequate for synthesizing a time-reversal symmetric single-photon wave packet.

III. SYMMETRIC SINGLE-PHOTON WAVE PACKET AND STATE TRANSFER

We demonstrate the performance of our protocol with chain-coupled microring resonators (MRRs) in Fig. 2(a) as the cavity cluster. Routinely used in integrated photonics [36,41–44], a MRR is known to support two degenerate modes, i.e., clockwise and counterclockwise whispering gallery modes (WGMs). An emitter with a linearly polarized dipole at the sending node couples equally with each WGM of the first MRR and the WGMs of the Nth MRR funnel to the waveguide in the form of single-photon wave packet, which subsequently propagates and excites the emitter in the identical receiving quantum node, completing the state-transfer process. The coupling of the emitter to the clockwise and counterclockwise WGMs in the MRRs is symmetric and eventually the emission outputs to both directions of the waveguide. The dynamics of the whole system can be solved by the same procedure developed in the previous section with a modified Hamiltonian considering two modes per MRR. As formulated in detail in Appendix B, the updated Hamiltonian includes

the energies of an additional set of modes and various couplings, such as the emitter-cavity coupling, mode-mode couplings, and mode-waveguide coupling. The formulation is shown in Appendix B to be formally equivalent to the case with one mode per cavity as proved in Appendix B. For the chain-coupled configuration, the coefficient α_n in Eq. (4) can be obtained analytically as $\alpha_n = -i\sqrt{2\kappa}g(\prod_{m=1}^{N-1} J_{m,m+1})/[(\prod_{m,m\neq n}^{N+1}(\Omega_n - \Omega_m)]$ (see derivations in Appendix C). We focus on practical situations of MRR arrays with number $N = 1 \sim 3$. Moreover, for conciseness we first consider only the resonant case $\omega_n = \omega_0$ and neglect the losses $\Gamma_0 = \Gamma_C = 0$. Later we explicitly discuss various imperfections, including the intrinsic losses of the TLS and cavities as well as detuning.

We scan the coupling rates in the realistic ranges and the resulting β-factor distributions are summarized in Fig. 2. For $N = 1$, the symmetry factor in Fig. 2(b) approaches 0.54 when the TLS-MRR coupling is either very strong or very weak. The emitted pulse gets the maximal symmetry factor of 0.9 when $\kappa = 3.3g$. For $N = 2$, we sweep the intercavity coupling rate J_{12} and the out-coupling rate κ. The results are coded in the color map of Fig. 2(c). The contours of $\beta = 0.54$, 0.90, and 0.97 are overlaid on the map. One can see the β factor exceeds 0.9 in a large area, and even reaches 0.97 at the optimal coupling rates $(J_{12}, \kappa) = (2.3, 6.2)g$. Finally, Fig. 2(d) displays β in color-coded contours for $N = 3$ as a function of three normalized coupling rates $(J_{12}, J_{23}, \kappa)/g$. Part of the parameter space is enlarged and visualized with the contours of $\beta = 0.9$, 0.97, and 0.99. The maximum value of $\beta = 0.993$ is obtained at $(J_{12}, J_{23}, \kappa)/g = (1.9, 2.9, 7.9)$. As expected,

the symmetry factor can be systematically improved by including more MRRs in a quantum node. This series of results also reveals to us that $N = 3$ could be a practical trade-off enabling a near-unity symmetry factor with only a few MRRs.

The pulse synthesis can be understood by adopting the physical picture of eigenstate superposition. We compute the eigenstates of the optimized $N = 3$ quantum node and find that the system splits into two pairs of states with eigenvalues of $\Omega_{1,2} = (\pm 2.73 - 0.87i)g$ and $\Omega_{3,4} = (\pm 0.93 - 1.11i)g$, respectively. To intuitively understand the result, we plot in Fig. 2(e) the time evolution of the normalized complex probability amplitude $\tilde{e}(t)$ and the components $e_n(t)$ from the four independent emitting states. One observes that the imaginary part of each channel destructively cancels to zero. The real part adds up to the final more symmetric $\tilde{e}(t)$, although each individual emitting state shows Rabi-like oscillations with an exponential decay. The four different emitting states with distinct phases, amplitudes, and Rabi frequencies synthesize a pulse with a near-unity symmetry factor.

We have thoroughly studied the process of sending one excitation of a node into the waveguide a time symmetric single-photon wave packet. In the following, we examine the receiving process. With an arbitrary incoming single-photon probability amplitude $f(t)$ in the waveguide, the dynamics of the receiving process $c_0(t)$ and $c_n(t)$ can be obtained by solving Eq. (3) with the drive term $\mathbf{d} = [0, 0, \ldots, -i\sqrt{\kappa}f(t)]^T$. Our modeling thus allows access to the whole quantum-state-transfer dynamic process, including the emission process with one excitation in the TLS, the propagation of single-photon wave packet along the waveguide and the excitation of the receiving node with the single-photon wave packet $f(t) = e(t)$. When the population of the TLS reaches the maximum $|c_0(t_f)|^2$, the receiving process completes. To evaluate the performance of state transfer, we define the maximum normalized population of the TLS $|\tilde{c}_0(t_f)|^2 = |c_0(t_f)|^2/|p_1|^2$ in the receiving node as the overall success rate R_s, which can be proved equal to the symmetry factor (see Appendix D).

For the chain-coupled MRR-based quantum nodes, Fig. 3(a) illustrates one possible realization towards near-unity state transfer. The emission from the sending node couples to the two identical branches of waveguide, transports and combines at the receiving node. The dynamics of the whole quantum-state-transfer process between the two quantum nodes are shown in Fig. 3 for $N = 1 \sim 3$ at the optimal coupling rates. In each graph, the time evolution of the sending, transport, and receiving processes are demonstrated with various traces in light blue, green, and pinkish shaded regions, respectively. Overall success rates of 0.905, 0.975, and 0.993 are achieved for the nodes with $N = 1 \sim 3$, respectively. For the quantum node with $N = 3$ in Fig. 3(d), as expected, the single-photon wave packet in the waveguide (green shaded) becomes
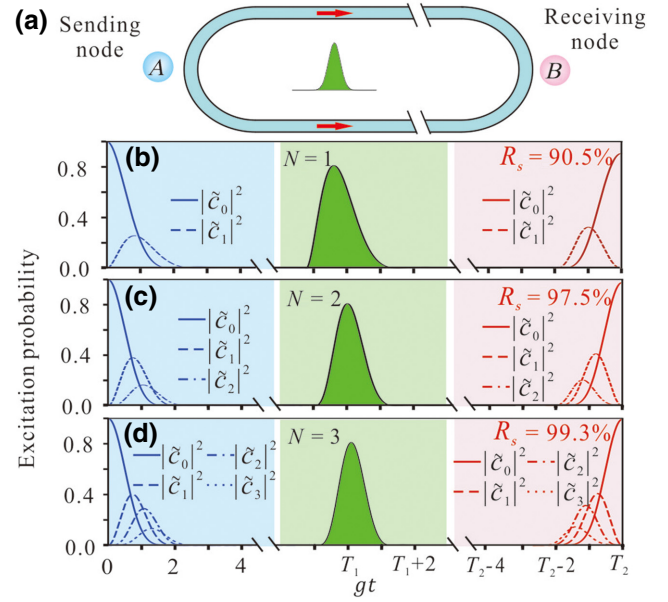

FIG. 3. (a) Schematic diagram of a complete state-transfer process between two identical chain-coupled MRR-based quantum nodes; (b)–(d) time evolution of normalized excitation probabilities of various channels $|\tilde{c}_i(t)|^2 = |c_i(t)|^2/|p_1|^2$ for $N = 1 \sim 3$. Sending, transport, and receiving processes are shown in light blue, green, and pinkish sections, respectively.

highly symmetric in time and thus can excite the identical quantum node with maximum probability according to the time-reversal symmetry [14,15]. In this case, one also clearly observes time-reversal symmetry of the entire state-transfer process, including the emission (sending) and the absorption (receiving) processes.

IV. TOLERANCE TO IMPERFECTIONS

We show that the proposed hybrid quantum node can secure a near-unity overall success rate of state transfer under ideal conditions. Here we discuss the tolerance of the protocol to imperfections relevant to the experimental realization, including the radiative losses of the TLS and MRR, MRR-TLS resonance detuning and cross-coupling between the two degenerate WGMs. The effects of the imperfections on the optimal overall success rate are evaluated quantitatively for the series of MRR-chain quantum nodes. First, we introduce separately radiative losses of the TLS and MRR in the range of $(0, 0.05)g$ to the optimized quantum nodes and examine the effects on the performance. The results of the overall success rate R_s depicted in Figs. 4(a) and 4(b) show that all the quantum nodes still retain remarkable performance. As discussed shortly in the experimental realization, the typical values of $\Gamma_0/2\pi$ and $\Gamma_C/2\pi$ are about 30 MHz amounting to $\Gamma_{0/C}/g \approx 0.013$ (with $g/2\pi \approx 2.3$ GHz) and have been indicated with the vertical dashed lines in Figs. 4(a) and 4(b). The success rate reduction due to such a level of loss rate for each
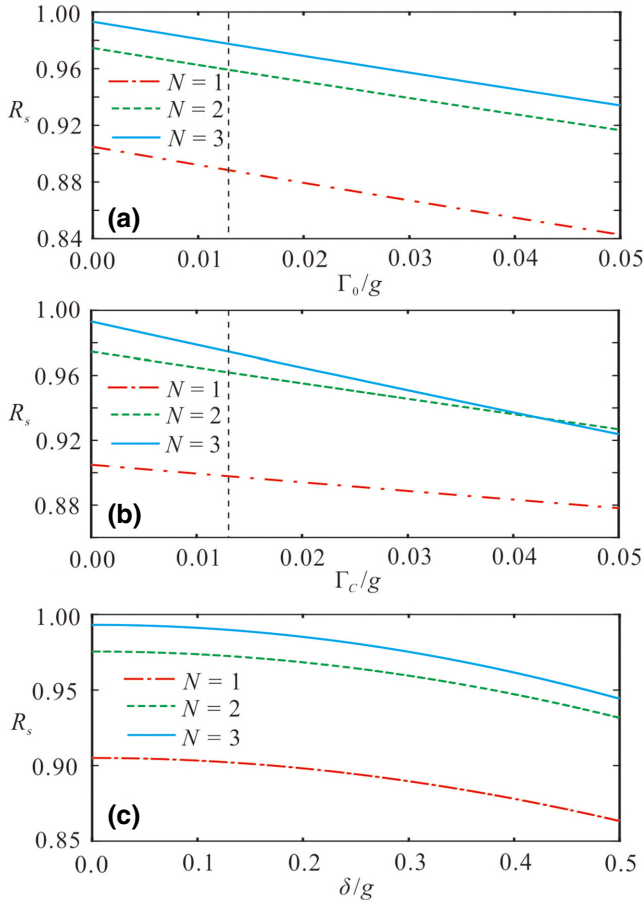
FIG. 4. Effects of nonideal conditions on the overall success rate for the chain-coupled MRR-based quantum node with $N = 1 \sim 3$ are plotted as functions of the radiative losses of (a) the TLS and (b) MRR, and (c) MRR-TLS resonance detuning or cross-coupling energy of the clockwise and counterclockwise WGMs. The typical values of Γ_0 and Γ_C are indicated with the vertical dashed lines.

postfabrication trimming [45] and MEMS actuation [46]. Additionally, scattering by roughness on the waveguide may degrade the performance of state transfer by inducing cross-coupling between degenerate WGMs. Theoretically, the cross-coupling can be described by adding an extra term $\hbar h_n \hat{a}_n^\dagger \hat{b}_n + $ H.c. in the Hamiltonian, where h_n is the cross-coupling rate, and $\hat{a}_n^\dagger$ ($\hat{a}_n$) and $\hat{b}_n^\dagger$ ($\hat{b}_n$) the creation (annihilation) operators of the degenerate WGMs. As shown in Appendix B, the cross-coupling rate h_n appears together with the detuning δ_n in the form of $\delta_n + h_n$ (for $n = 1 \sim N$) in the resulting Hamiltonian matrix **H**. Therefore, its effect is the same as the detuning, as shown in Fig. 4(c), and turns out practically negligible with typical rates reported for high-quality-factor cavities [36,47]. When the typical loss rates are assumed and other imperfections carefully brought under control, calculations showing a success rate of 95.7% can be expected.

V. DISCUSSION ON EXPERIMENTAL REALIZATION

Next we discuss possible experimental realizations of the hybrid quantum node. We explore the feasibility of the silicon-nitride (SiN) platform for building the photonic circuits and germanium vacancy (GeV) centers in nanodiamond [4,48,49] as solid-state emitters. The SiN platform has the advantages of having ultralow waveguide propagation loss (as low as 0.1 dB/m) in the visible and near-infrared range [36,37,43]. GeV centers are attractive due to near-unity quantum yield, nonblinking emission, excellent photostability, and lifetime-limited emission linewidth (about 30 MHz) at cryogenic temperatures. As schematically displayed in Figs. 5(a) and 5(b), one may fabricate MRRs based on a SiN slot waveguide on silica with a radius of about 8 μm. The rectangular slot waveguide

curve is seen to be less than 2%. Improved emitter-cavity coupling promised by optimal resonator and waveguide designs, including MRR, microdisk, and microsphere resonators, may help to mitigate the influence.

Besides the radiative losses, fabrication imperfections may also cause resonance detuning $\delta = \omega_n - \omega_0$, which is assumed homogeneous among the MRRs for simplicity. The theoretical analysis procedure developed in the previous sections can be equally applied to study situations with inhomogeneous resonance detuning. The dotted, dashed, and solid traces in Fig. 4(c) depict the dependences of the overall success rate R_s on the detuning for $N = 1$, 2, and 3, respectively. One sees that the influence is mild and pretty high R_s can still be obtained even for $\delta = 0.5g$. We emphasize that the effect of detuning can be effectively minimized in practice, as the emitter transition frequency can be fine tuned via Stark effect and the cavity resonances could also be tuned by various techniques such as
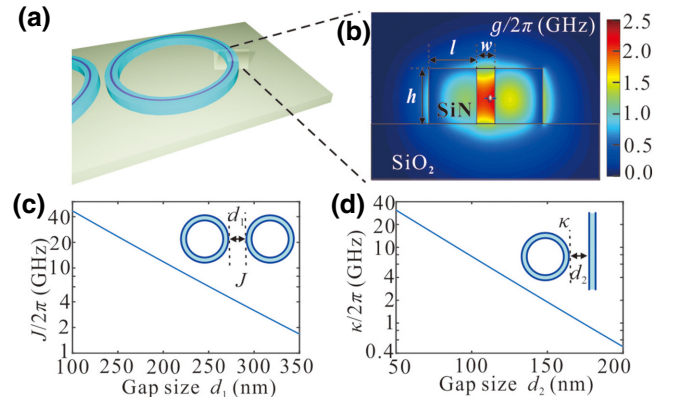

FIG. 5. (a) A sketch of the node based on SiN slot waveguide microring resonators and embedded quantum emitters; (b) TLS-MRR coupling constant g distribution; Semilog plots of (c) MRR-MRR coupling rate J and (d) MRR-waveguide coupling rate κ as functions of the gap sizes.

cross section is specified by $(w, l, h) = (80, 210, 230)$ nm and the slot can be filled by resin with nanodiamond embedded [49,50]. Such a kind of MRR could provide intrinsic quality factors in the order of 10^7 ($\Gamma_C \sim 30$ MHz). The TLS-MRR coupling constant can be calculated as $g = 0.5\sqrt{3\lambda^2 c \Gamma_0/(2\pi n^3 V_{\text{eff}})}$, where λ, c, n, V_{eff} are the emission wavelength in vacuum, speed of light, refractive index of the matrix, and the effective mode volume (see Appendix E), respectively. Figure 5(b) shows a color-coded map of g on the cross section of the waveguide. Coupling constants of a few GHz are achievable. For the $N = 3$ node with the optimal parameters of $(J_{12}, J_{23}, \kappa)/g = (1.9, 2.9, 7.9)$, the emission of the GeV centers will be delivered to the waveguide with efficiencies up to about 99% due to enhanced emission by the MRR resonance and large MRR-waveguide out-coupling rate. Based on the above basic configuration, we examine the achievable parameter ranges of MRR-MRR coupling rate J and MRR-waveguide coupling rate κ, which can be calculated semianalytically (see Appendix E). Figure 5(c) [Fig. 5(d)] depicts the coupling rate J (κ) as a function of MRR-MRR (MRR-waveguide) gap size. The TLS-MRR coupling constant g is only slightly modified due to the small changes of V_{eff} in the presence of coupling. One clearly observes that the required J and κ are feasible at realistic gap sizes and their values are orders of magnitude greater than the radiation loss of the MRRs. In the MRR-based configuration, phase stability of the two paths to the receiving node is required and could be maintained as a merit of the integrated photonic platform. In practice, phase-tuning units along the paths could be applied to ensure that the emitter in the receiving node is at an antinode of the two WGMs. The guidelines and the designs given here are to demonstrate the experimental feasibility for nearly perfect on-chip quantum state transfer. Alternative cavity structures, matter-based quantum systems and design strategies could certainly be explored for other experimental realizations.

VI. CONCLUSION

We theoretically propose and systematically investigate a category of hybrid quantum nodes comprising a single matter-based quantum system and a couple-cavity cluster towards perfect state transfer between nodes on a photonic chip. Our scheme for state transfer relies on the synthesis of a time-reversal symmetric single-photon wave packet through optimizing the interference (superposition) of the eigenstates of the hybrid node. With a chain of three microring resonators as an example of the cavity cluster, we demonstrate, in principle, that the hybrid node allows for 99% overall success rate in deterministically transferring a state between two nodes. We remark that the MRR-based configuration is just one exemplary implementation and alternative schemes based on cavities with unidirectional out coupling [51,52] should also work. The scheme

is static without the need for any dynamic modulation and could be implemented on CMOS-compatible integrated photonic platforms [35,37,53], promising scaling up the size of the system at affordable resources. In a wider context, our work enables the complete transfer of an elementary excitation between two distant systems through a propagating wave packet, and is extendable to other types of systems, for instance, superconducting qubits [54–56] and optomechanical systems [57], which are highly promising platforms for quantum information processing. It is also applicable for efficiently interfacing heterogeneous quantum systems, such as single molecules in solid-state matrix and trapped cold atoms [58], nitrogen vacancy centers and superconducting qubits [59], and acoustic and superconducting qubits [60,61]. We believe our work paves the way for chip-scale elementary excitation transfer in a variety of network systems.

APPENDIX A: ELIMINATION OF THE WAVEGUIDE CONTINUUM UNDER THE WEISSKOPF-WIGNER APPROXIMATION

In the main text we present the dynamical equations of the composite quantum node based on a coupled-cavity system. Here we provide a supplementary treatment on the elimination of waveguide continuum from the system dynamics by using Weisskopf-Wigner approximation [62]. We start with substituting the wave function, Eq. (2), of the main text into the Schrödinger equation in the interaction picture. The probability amplitudes in the wave function are then found to satisfy the following system of differential equations:

$$i\partial_t c_0 = (-i\Gamma_0/2)c_0 + g c_1, \tag{A1}$$

$$i\partial_t c_1 = (\delta_1 - i\Gamma_C/2)c_1 + g c_0 + \sum_{m=2}^{N} J_{1,m} c_m, \tag{A2}$$

$$i\partial_t c_n = (\delta_n - i\Gamma_C/2)c_n + \sum_{m=1, m\neq n}^{N} J_{n,m} c_m, \quad (n = 2, \ldots, N-1), \tag{A3}$$

$$i\partial_t c_N = (\delta_N - i\Gamma_C/2)c_N + \sum_{m=1}^{N-1} J_{N,m} c_m + \sum_{k>0} V_k c_k e^{-i(\omega_k - \omega_0)t} \tag{A4}$$

$$i\partial_t c_k = V_k c_N e^{i(\omega_k - \omega_0)t}. \tag{A5}$$

To eliminate the waveguide continuum in Eq. (A4), we replace c_k with the integration of Eq. (A5) and get

$$i\partial_t c_N = (\delta_N - i\Gamma_C/2)c_N + \sum_{m=1}^{N-1} J_{N,m}c_m + I, \quad (A6)$$

with

$$I = \sum_k V_k e^{-i(\omega_k-\omega_0)t}\left[-iV_k \int_0^t c_N(t')e^{i(\omega_k-\omega_0)t'}dt' + c_k(0)\right]. \quad (A7)$$

Here the waveguide modes are formally defined in a segment of waveguide of finite but macroscopic length L, so that the spectrum is in practice continuous and consequently the summation in Eq. (A7) over k converts to an integral, i.e., $\sum_k \rightarrow L/2\pi \int_0^\infty dk$. Our proposed quantum node works within a very narrow bandwidth relative to the dispersion of the waveguide modes, such that the dispersion can be linearized around the central frequency ω_c and the corresponding wave vector k_c, i.e., $k - k_c \approx (\omega_k - \omega_c)/v_g$ (v_g is the group velocity). This condition on bandwidth is equivalent to the assumption that the temporal evolution of c_N is much slower than that of the waveguide modes, which is the standard assumption of Weisskopf-Wigner approximation for studying atomic spontaneous decay. Using the linearization the integration variable k can be changed to ω_k. After these operations, Eq. (A7) is reformulated as $I = I_1 + I_2$ with

$$I_1 = \frac{-iL}{2\pi v_g} \int_0^t c_N(t')dt' \int_0^\infty V_k^2 e^{i(\omega_k-\omega_0)(t'-t)}d\omega_k, \quad (A8)$$

$$I_2 = \frac{L}{2\pi v_g} \int_0^\infty c_k(0)V_k e^{-i(\omega_k-\omega_0)t}d\omega_k. \quad (A9)$$

The narrow bandwidth also implies very weak wave-vector dependence of the coupling rates, and justifies the approximation $V \equiv V_k$. Moreover, the finite integration range of ω_k can be extended to $(-\infty, \infty)$ considering the limited bandwidth. Under these approximations the integral I_1 is simplified into

$$I_1 = \frac{-iV^2 L}{2v_g}c_N(t) \equiv -i\frac{\kappa}{2}c_N(t). \quad (A10)$$

One can see the coupling to the waveguide continuum amounts to an irreversible energy transfer from the Nth cavity to the waveguide with an effective rate $\kappa = V^2 L/v_g$. The integral I_2 represents an external input from the

waveguide and leads to the definition of input pulse

$$f(t) \equiv I_2/\sqrt{\kappa} = \frac{\sqrt{L/v_g}}{2\pi}\int_{-\infty}^\infty c_k(0)e^{-i(\omega_k-\omega_0)t}d\omega_k. \quad (A11)$$

At last we substitute $I = I_1 + I_2$ back to Eq. (A6) and obtain the dynamical equation for c_N,

$$i\partial_t c_N = (\delta_N - i\Gamma_C/2 - i\kappa/2)c_N + \sum_{m=1}^{N-1} J_{N,m}c_m + \sqrt{\kappa}f. \quad (A12)$$

Now the waveguide continuum is decoupled from the coupled cavity system, whose dynamics is governed by the Eqs. (A1) to (A3) and (A12). They are rewritten in a compact form as Eq. (3) of the main text. Additionally, the photon pulse $e(t)$ in the waveguide consists of the emission from the Nth cavity and possibly an external input, and therefore can be expressed as

$$e(t) = f(t) - i\sqrt{\kappa}c_N(t). \quad (A13)$$

APPENDIX B: FORMULATION FOR THE CASE OF ONE CAVITY WITH TWO MODES

The general formulation of the hybrid quantum node in the paper assumes single-mode description for each cavity. In view that a MRR has two degenerate WGMs, here we show the MRR-based quantum nodes can be treated equivalently with the single-mode formulation. A MRR supports two degenerate modes denoted by annihilation (creation) operators $\hat{a}$ ($\hat{a}^\dagger$) and $\hat{b}$ ($\hat{b}^\dagger$), respectively. The MRR-chain quantum node as shown in Fig. 2(a) in the main text is then described by the Hamiltonian

$$\hat{H} = \hat{H}_0 + \hat{H}_{AM} + \hat{H}_{MM} + \hat{H}_{MW}, \quad (B1)$$

consisting of the uncoupled Hamiltonian $\hat{H}_0/\hbar = (\omega_0 - i\Gamma_0/2)\hat{\sigma}_+\hat{\sigma}_- + \sum_{n=1}^N(\omega_n - i\Gamma_C/2)(\hat{a}_n^\dagger\hat{a}_n + \hat{b}_n^\dagger\hat{b}_n) + \sum_k \omega_k \hat{c}_k^\dagger\hat{c}_k$, The TLS-MRR coupling $\hat{H}_{AM}/\hbar = g(\hat{\sigma}_+\hat{a}_1 + \hat{\sigma}_+ \hat{b}_1 + \text{H.c.})$, intermode coupling $\hat{H}_{MM}/\hbar = \sum_{n=1}^{N-1} J_{n,n+1} (\hat{a}_n^\dagger\hat{b}_{n+1} + \hat{a}_{n+1}^\dagger\hat{b}_n + \text{H.c.}) + \sum_{n=1}^N(h_n\hat{a}_n^\dagger\hat{b}_n + \text{H.c.})$ and MRR-waveguide coupling $\hat{H}_{MW}/\hbar = \sum_k(V_k\hat{a}_N^\dagger\hat{c}_{k-} + V_k \hat{b}_N^\dagger\hat{c}_{k+} + \text{H.c.})$. The waveguide modes propagating in opposite directions are characterized with the wave vectors $k_\pm$. Herein the intercoupling h_n [63,64] accounts for the cross-coupling between the degenerate WGMs of MRR.

We describe the state of the system in the interaction picture rotating at ω_0 with the wave function

$$|\psi\rangle = \Bigg[c_0(t)\hat{\sigma}_+ + \sum_{n=1}^{N}[c_{n,a}(t)\hat{a}_n^\dagger + c_{n,b}(t)\hat{b}_n^\dagger]$$

$$+ \sum_k c_k(t)\hat{c}_k^\dagger\Bigg]|\varnothing\rangle. \tag{B2}$$

Then its evolution is determined by the Schrödinger equation $i\hbar\partial_t|\psi\rangle = \hat{\mathcal{V}}|\psi\rangle$ with $\hat{\mathcal{V}}$ being the interaction Hamiltonian deduced from $\hat{H}$. Applying the Weisskopf-Wigner approximation [7,62,65] we obtain the evolution equations for the coefficients

$$i\partial_t c_0 = (-i\Gamma_0/2)c_0 + gc_{1,a} + gc_{1,b}, \tag{B3}$$

$$i\partial_t c_{1,a} = (\delta_1 - i\Gamma_C/2)c_{1,a} + gc_0 + J_{1,2}c_{2,b} + h_1 c_{1,b}, \tag{B4}$$

$$i\partial_t c_{1,b} = (\delta_1 - i\Gamma_C/2)c_{1,b} + gc_0 + J_{1,2}c_{2,a} + h_1 c_{1,a}, \tag{B5}$$

$$i\partial_t c_{n,a} = (\delta_n - i\Gamma_C/2)c_{n,a} + J_{n,n+1}c_{n+1,b} + J_{n-1,n}c_{n-1,b}$$
$$+ h_n c_{n,b}, \quad n = 2 \sim N - 1, \tag{B6}$$

$$i\partial_t c_{n,b} = (\delta_n - i\Gamma_C/2)c_{n,b} + J_{n,n+1}c_{n+1,a} + J_{n-1,n}c_{n-1,a}$$
$$+ h_n c_{n,a}, \quad n = 2 \sim N - 1, \tag{B7}$$

$$i\partial_t c_{N,a} = (\delta_N - i\Gamma_C/2 - i\kappa/2)c_{N,a} + J_{N-1,N}c_{N-1,b}$$
$$+ h_N c_{N,b} + \sqrt{\kappa}f_-, \tag{B8}$$

$$i\partial_t c_{N,b} = (\delta_N - i\Gamma_C/2 - i\kappa/2)c_{N,b} + J_{N-1,N}c_{N-1,a}$$
$$+ h_N c_{N,a} + \sqrt{\kappa}f_+, \tag{B9}$$

where κ is the coupling rate between the WGM and the waveguide. Note that in the formulation here we allow possible external input wave packets $f_\pm(t)$. The output pulses in opposite directions of the waveguide then can be expressed with an input-output form as [66]

$$e_-(t) = f_-(t) - i\sqrt{\kappa}c_{N,a}(t), \tag{B10}$$

$$e_+(t) = f_+(t) - i\sqrt{\kappa}c_{N,b}(t). \tag{B11}$$

We assume the various coupling rates in the above formulation are symmetric with respect to the clockwise and counterclockwise WGMs, and only symmetric input $[f_-(t) = f_+(t)]$ is considered. The coefficients thus exhibit the same symmetry $c_{n,a}(t) = c_{n,b}(t)$, which allows us to define the effective amplitudes $c_n(t) = \sqrt{2}c_{n,a}(t)$ and effective input $f(t) = \sqrt{2}f_-(t)$ and output $e(t) = \sqrt{2}e_-(t)$. Expressed in terms of the effective variables, the evolution equations can be written compactly in matrix form as Eq. (3) of the main text. Therein the Hamiltonian $\mathbf{H} = \text{tridiag}[\mathbf{u}, \mathbf{v}, \mathbf{u}]$ with

$\mathbf{u} = (\sqrt{2}g, J_{12}, J_{23}, \ldots, J_{N-1,N})$ and $\mathbf{v} = (-i\Gamma_0/2, \delta_1 + h_1 - i\Gamma_C/2, \delta_2 + h_2 - i\Gamma_C/2, \ldots, \delta_N + h_N - i\Gamma_C/2 - i\kappa/2)$. One can see that this Hamiltonian assumes the same form as that of a chain-coupled N single-mode cavities except that the effective TLS-cavity coupling strength becomes $\sqrt{2}g$. This justifies the treatment of the MRR-based quantum nodes with the single-mode formulation.

APPENDIX C: DERIVATION OF α_n

In this appendix we derive the expression of α_n for the chain-coupled MRR-based quantum node by solving Eq. (3) in the main text with the initial condition of $\mathbf{c}(0) = [p_1, 0, \ldots, 0]^T$ and $\mathbf{d} = 0$. In particular, we apply the Laplace transform $\mathcal{L}[f](s) = \int_0^\infty f(t)e^{-st}dt$ to the evolution equation and transform it into a system of algebraic equations in the matrix form as

$$(s\mathbf{I} + i\mathbf{H})\mathbf{c}(s) \equiv \mathbf{T}\mathbf{c}(s) = \mathbf{c}(0). \tag{C1}$$

Here $\mathbf{T}$ is a symmetric tridiagonal matrix and its inverse admits an analytical form:

$$(T^{-1})_{m,n} = \begin{cases} (-1)^{m+n}\displaystyle\prod_{q=m}^{n-1} T_{q,q+1}\dfrac{d_{n+1}\cdots d_{N+1}}{\delta_m\cdots\delta_{N+1}}, & m \le n \\[6mm] (-1)^{n+m}\displaystyle\prod_{q=n}^{m-1} T_{q,q+1}\dfrac{d_{m+1}\cdots d_{N+1}}{\delta_n\cdots\delta_{N+1}}, & m > n \end{cases}, \tag{C2}$$

which depends on two recurrence sequences $\{d_n\}$ and $\{\delta_n\}$ [67]. Since the emitted pulse has the amplitude $e(t) = -i\sqrt{\kappa}c_N(t)$, we need only to find $c_N(s) = p_1(T^{-1})_{N+1,1}$. By using Eq. (C2) and the relation $\delta_1\delta_2\cdots\delta_{N+1} = \det\{\mathbf{T}\}$ [67], we obtain

$$(T^{-1})_{N+1,1} = (-1)^N\frac{T_{1,2}\cdots T_{N,N+1}}{\det\{\mathbf{T}\}}. \tag{C3}$$

Alternatively the determinant of $\mathbf{T} = s\mathbf{I} + i\mathbf{H}$ can be expressed as $\det\{\mathbf{T}\} = \prod_{n=1}^{N+1}(s + i\Omega_n)$, where Ω_n is the nth eigenvalue of $\mathbf{H}$. Then Eq. (C3) is further altered to give

$$c_N(s) = p_1(-1)^N\frac{T_{1,2}\cdots T_{N,N+1}}{\prod_{n=1}^{N+1}(s + i\Omega_n)}. \tag{C4}$$

Now we find the coefficient $c_N(t)$ by applying inverse Laplace transform

$$c_N(t) = \mathcal{L}^{-1}\{c_N(s)\}$$

$$= p_1 i^{-N}\prod_{q=1}^{q=N} T_{q,q+1}\sum_{n=1}^{N+1}\frac{e^{-i\Omega_n t}}{\prod_{m=1,m\ne n}^{N+1}(\Omega_n - \Omega_m)}. \tag{C5}$$

For the MRR-chain quantum nodes $T_{12} = i\sqrt{2}g$, $T_{23} = iJ_{12}, \ldots, T_{n,n+1} = iJ_{n-1,n}$, thus

$$c_N(t) = p_1 \sum_{n=1}^{N+1} \frac{\sqrt{2}g \prod_{m=1}^{N-1} J_{m,m+1}}{\prod_{m=1,m\neq n}^{N+1}(\Omega_n - \Omega_m)} e^{-i\Omega_n t}. \quad \text{(C6)}$$

Comparing $e(t) = -i\sqrt{\kappa}c_N(t)$ with Eq. (4) of the main text, we finally arrive at

$$\alpha_n = \frac{-i\sqrt{2\kappa}g \prod_{m=1}^{N-1} J_{m,m+1}}{\prod_{m=1,m\neq n}^{N+1}(\Omega_n - \Omega_m)}. \quad \text{(C7)}$$

APPENDIX D: PROOF OF THE EQUALITY BETWEEN β AND R_s

To quantify the pulse symmetry, we introduce symmetry factor β in the main text. β is defined as the maximal overlap integral between a certain pulse and its time-reversed copy with a variable time shift t_0. We now show that the success rate R_s equals β. The time evolution of the whole system is described by Eq. (3) in the main text, whose formal solution can be expressed in a matrix form as follows [68]:

$$\mathbf{c}(t) = e^{-i\mathbf{H}t}\left(\mathbf{c}(0) + \int_0^t e^{i\mathbf{H}t'} \cdot \mathbf{d} \cdot dt'\right), \quad \text{(D1)}$$

where $\mathbf{c}(0)$ is the initial condition for $\mathbf{c}(t)$. $e^{-i\mathbf{H}t}$ would be an $(N+1) \times (N+1)$ matrix

$$e^{-i\mathbf{H}t} = \mathbf{M}(\mathbf{t}). \quad \text{(D2)}$$

Since $\mathbf{H}$ is a symmetric matrix for our system, $\mathbf{M}(t)$ is naturally also symmetric, i.e., $M_{m,n}(t) = M_{n,m}(t)$. For the emission process of the system, the TLS is initially in the superposition state $(p_1\hat{\sigma}_+^A + p_0)|g_A\rangle$, then $\mathbf{c}(0) = [p_1, 0, \ldots, 0, 0]^T$ and $\mathbf{d} = 0$. The solution reduces to

$$\mathbf{c}(t) = e^{-i\mathbf{H}t}[p_1, 0, \ldots, 0, 0]^T. \quad \text{(D3)}$$

Then $c_N(t)$ can be expressed as follows:

$$c_N(t) = M_{N+1,1}(t) = \frac{i}{\sqrt{\kappa}}e(t), \quad \text{(D4)}$$

where in the last step we use the relation $e(t) = -i\sqrt{\kappa}c_N(t)$ given in Appendix A. For the receiving process, the input pulse $f(t) = e(t)$ and the dynamics is determined by solving Eq. (D1) with the drive $\mathbf{d} = [0, 0, \ldots, 0, -i\sqrt{\kappa}e(t)]^T$

and the initial condition $\mathbf{c}(0) = 0$. The solution reads

$$\mathbf{c}(t) = \int_0^t e^{-i\mathbf{H}(t-t')} \cdot \mathbf{d}dt'$$

$$= \int_0^t \mathbf{M}(t-t') \cdot [0, 0, \ldots, 0, -i\sqrt{\kappa}e(t)]^T dt'. \quad \text{(D5)}$$

The excitation amplitude of the atom in the receiving node thus turns out

$$c_0(t) = \int_0^t M_{1,N+1}(t-t') \cdot [-i\sqrt{\kappa}e(t')]dt'$$

$$= \int_0^t M_{N+1,1}(t-t') \cdot [-i\sqrt{\kappa}e(t')]dt'$$

$$= \int_0^t \frac{i}{\sqrt{\kappa}}e(t-t') \cdot [-i\sqrt{\kappa}e(t')]dt'$$

$$= \int_0^t e(t-t')e(t')dt'. \quad \text{(D6)}$$

By definition the success rate is the maximum of $|c_0(t)/p_1|^2$, and becomes

$$R_s = \max_t\left(\left|\int_0^t e(t')e(t-t')dt'/p_1^2\right|^2\right). \quad \text{(D7)}$$

On the other hand, the β factor defined in the main text can be reformulated by realizing that the emitted pulse in quantum state transfer strictly has amplitude of zero before emission starts. The integrand in the definition of β factor is thus nonzero only in a finite range. We specifically include Heaviside function $\Theta(t)$ in the integral and get

$$\beta = \max_{t_0}\left(\left|\int_0^{2t_0} \Theta(t)e(t)\Theta(2t_0 - t)e(2t_0 - t)dt/p_1^2\right|^2\right)$$

$$= \max_{t_0}\left(\left|\int_0^{2t_0} e(t)e(2t_0 - t)dt/p_1^2\right|^2\right) = R_s. \quad \text{(D8)}$$

APPENDIX E: EVALUATION OF THE COUPLING RATES FOR REALISTIC WAVEGUIDE AND CAVITY STRUCTURES

We discuss the guidelines to the experimental realization of our proposal. In this appendix, more details are provided regarding the estimation of the coupling rates including g, J, and κ.

The coupling strength g of the emitter with the first MRR is calculated according to Ref. [64]

$$g = \frac{1}{2}\sqrt{\frac{3}{2\pi}\frac{\lambda^2 c}{n^3 V_{\text{eff}}}\Gamma_0}, \quad \text{(E1)}$$

where the emitter with a transition corresponding to a free-space wavelength $\lambda = 602$ nm is located at $\mathbf{x_0}$ in the

dielectric of refractive index n. $V_{\text{eff}} = 2\pi R S_{\text{eff}}$ is the mode volume of the whispering gallery mode in the MRR of radius R. The effective mode area is in turn obtained with

$$S_{\text{eff}} = \frac{\iint \varepsilon |\mathbf{E}|^2 dS}{\varepsilon |\hat{\mathbf{d}} \cdot \mathbf{E}(\mathbf{x}_0)|^2}, \quad (E2)$$

where the mode profile $\mathbf{E}$ is found numerically with the finite-element method. In particular, we work with a horizontally oriented emitter with decay rate $\Gamma_0 = 30$ MHz $\times 2\pi$. Following the above procedures, the distribution of the coupling strength g for the emitter is rendered as a color map in Fig. 5(b) of the main text when the emitter is located at arbitrary positions on the waveguide cross section.

As for the MRR-MRR (MM) and MRR-waveguide (MW) coupling rates J and κ, both can be estimated using the method proposed by Bahadori *et al.* [42]. Here we briefly outline the major steps to obtain the coupling rates. Firstly we find the guiding mode of the single slot waveguide at the wavelength $\lambda = 602$ nm. The effective index of the fundamental mode n_{eff} is 1.65. When two such slot waveguides are placed side by side, two super modes (of even and odd parity) form via fundamental mode coupling. Then we numerically calculate the effective indices of the super modes as functions of the gap size d between the two waveguides and fit the functions with the following expressions:

$$n_e = n_{\text{eff}} + a_e e^{-\gamma_e d}, \quad (E3)$$

$$n_o = n_{\text{eff}} - a_o e^{-\gamma_o d}, \quad (E4)$$

where the indices "e" and "o" indicate even and odd super modes, respectively. As displayed in Fig. 6, the fitted traces agree very well with the discrete data points. The fitted parameters are found to be $a_e = 0.0355$, $\gamma_e = 0.0162$ nm^{-1}, $a_o = 0.0139$, and $\gamma_o = 0.0113$ nm^{-1}. These parameters are needed for determining the dimensionless parameter

$$\kappa' = \sin\left(\frac{\pi}{\lambda}\left[\frac{a_e}{\gamma_e}e^{-\gamma_e d}B(x_e) + \frac{a_o}{\gamma_o}e^{-\gamma_o d}B(x_o)\right]\right), \quad (E5)$$

which is used in transfer matrix computation. Herein the functions $B(x_e)$ and $B(x_o)$ depend on the waveguide curvature in the specific coupling configuration, e.g., MM or MW. In particular, they can be approximated as

$$B_{\text{MW}}(x_{e/o}) \approx \sqrt{2\pi x_{e/o}}$$
$$= \sqrt{2\pi \gamma_{e/o}(R + W/2)}, \quad (E6)$$

$$B_{\text{MM}}(x_{e/o}) \approx 0.5 B_{\text{MW}}(2x_{e/o})$$
$$= 0.5\sqrt{2\pi \cdot 2x_{e/o}}$$
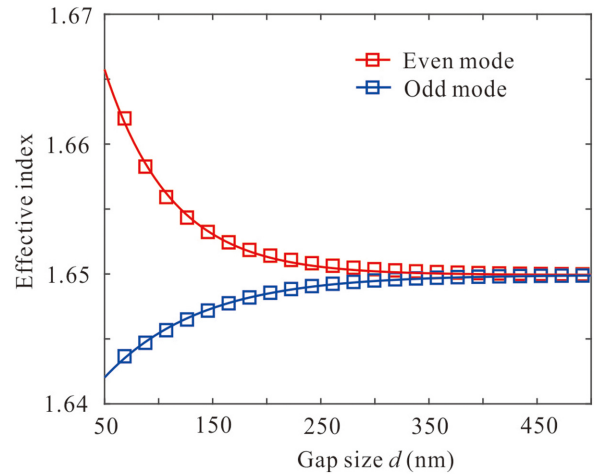$$= \sqrt{\pi \gamma_{e/o}(R + W/2)}, \quad (E7)$$

FIG. 6. The effective indices of the two super modes of two identical slot waveguides placed side by side are numerically calculated (markers) and analytically fitted (solid traces).

where $W = 2l + w$ is the full width of the slot waveguide. Finally the coupling rates κ and J can be expressed as [41]

$$\kappa = \frac{\kappa_{MW}'^2}{2\pi R}v_g, \quad (E8)$$

$$J = \frac{\kappa_{MM}'}{2\pi R}v_g, \quad (E9)$$

and the numerical results are presented in Figs. 5(c) and 5(d) in the main text.

[1] O. Benson, Assembly of hybrid photonic architectures from nanophotonic constituents, Nature **480**, 193 (2011).

[2] P. Lodahl, S. Mahmoodian, and S. Stobbe, Interfacing single photons and single quantum dots with photonic nanostructures, Rev. Mod. Phys. **87**, 347 (2015).

[3] A. W. Elshaari, W. Pernice, K. Srinivasan, O. Benson, and V. Zwiller, Hybrid integrated quantum photonic circuits, Nat. Photonics **14**, 285 (2020).

[4] N. H. Wan, T.-J. Lu, K. C. Chen, M. P. Walsh, M. E. Trusheim, L. De Santis, E. A. Bersin, I. B. Harris, S. L. Mouradian, I. R. Christen, E. S. Bielejec, and D. Englund, Large-scale integration of artificial atoms in hybrid photonic circuits, Nature **583**, 226 (2020).

[5] A. D. Greentree, C. Tahan, J. H. Cole, and L. C. L. Hollenberg, Quantum phase transitions of light, Nat. Phys. **2**, 856 (2006).

[6] J.-T. Shen and S. Fan, Theory of single-photon transport in a single-mode waveguide. I. Coupling to a cavity containing a two-level atom, Phys. Rev. A **79**, 023837 (2009).

[7] Y. Chen, M. Wubs, J. Mørk, and A. F. Koenderink, Coherent single-photon absorption by single emitters coupled to one-dimensional nanophotonic waveguides, New J. Phys. **13**, 103010 (2011).

[8] Z. Liao, X. Zeng, H. Nha, and M. S. Zubairy, Photon transport in a one-dimensional nanophotonic waveguide QED system, Phys. Scr. **91,** 063004 (2016).

[9] H. Zheng, D. J. Gauthier, and H. U. Baranger, Waveguide-QED-Based Photonic Quantum Computation, Phys. Rev. Lett. **111,** 090502 (2013).

[10] A. González-Tudela, V. Paulisch, H. J. Kimble, and J. I. Cirac, Efficient Multiphoton Generation in Waveguide Quantum Electrodynamics, Phys. Rev. Lett. **118,** 213601 (2017).

[11] H. J. Kimble, The quantum internet, Nature **453,** 1023 (2008).

[12] A. Reiserer and G. Rempe, Cavity-based quantum networks with single atoms and optical photons, Rev. Mod. Phys. **87,** 1379 (2015).

[13] D. Pinotsi and A. Imamoglu, Single Photon Absorption by a Single Quantum Emitter, Phys. Rev. Lett. **100,** 093603 (2008).

[14] M. Stobińska, G. Alber, and G. Leuchs, Perfect excitation of a matter qubit by a single photon in free space, Europhys. Lett. **86,** 14007 (2009).

[15] E. Rephaeli, J.-T. Shen, and S. Fan, Full inversion of a two-level atom with a single-photon pulse in one-dimensional geometries, Phys. Rev. A **82,** 033804 (2010).

[16] M. Bader, S. Heugel, A. L. Chekhov, M. Sondermann, and G. Leuchs, Efficient coupling to an optical resonator by exploiting time-reversal symmetry, New J. Phys. **15,** 123008 (2013).

[17] M. F. Yanik and S. Fan, Time Reversal of Light with Linear Optics and Modulators, Phys. Rev. Lett. **93,** 173903 (2004).

[18] L. Yuan, M. Xiao, and S. Fan, Time reversal of a wave packet with temporal modulation of gauge potential, Phys. Rev. B **94,** 140303(R) (2016).

[19] J. I. Cirac, P. Zoller, H. J. Kimble, and H. Mabuchi, Quantum State Transfer and Entanglement Distribution among Distant Nodes in a Quantum Network, Phys. Rev. Lett. **78,** 3221 (1997).

[20] T. Pellizzari, Quantum Networking with Optical Fibres, Phys. Rev. Lett. **79,** 5242 (1997).

[21] N. Trautmann, G. Alber, G. S. Agarwal, and G. Leuchs, Time-Reversal-Symmetric Single-Photon Wave Packets for Free-Space Quantum Communication, Phys. Rev. Lett. **114,** 173601 (2015).

[22] A. Baksic, H. Ribeiro, and A. A. Clerk, Speeding up Adiabatic Quantum State Transfer by Using Dressed States, Phys. Rev. Lett. **116,** 230503 (2016).

[23] R. Johne and A. Fiore, Single-photon absorption and dynamic control of the exciton energy in a coupled quantum-dot–cavity system, Phys. Rev. A **84,** 053850 (2011).

[24] B. Vogell, B. Vermersch, T. E. Northup, B. P. Lanyon, and C. A. Muschik, Deterministic quantum state transfer between remote qubits in cavities, Quantum Sci. Technol. **2,** 045003 (2017).

[25] S. Ritter, C. Nölleke, C. Hahn, A. Reiserer, A. Neuzner, M. Uphoff, M. Mücke, E. Figueroa, J. Bochmann, and G. Rempe, An elementary quantum network of single atoms in optical cavities, Nature **484,** 195 (2012).

[26] D. N. Matsukevich and A. Kuzmich, Quantum state transfer between matter and light, Science **306,** 663 (2004).

[27] N. Kalb, A. Reiserer, S. Ritter, and G. Rempe, Heralded Storage of a Photonic Quantum Bit in a Single Atom, Phys. Rev. Lett. **114,** 220501 (2015).

[28] O. Bechler, A. Borne, S. Rosenblum, G. Guendelman, O. E. Mor, M. Netser, T. Ohana, Z. Aqua, N. Drucker, R. Finkelstein, Y. Lovsky, R. Bruch, D. Gurovich, E. Shafir, and B. Dayan, A passive photon-atom qubit swap operation, Nat. Phys. **14,** 996 (2018).

[29] C. Liu, Y. Sun, L. Zhao, S. Zhang, M. M. T. Loy, and S. Du, Efficiently Loading a Single Photon into a Single-Sided Fabry-Perot Cavity, Phys. Rev. Lett. **113,** 133601 (2014).

[30] B. Srivathsan, G. K. Gulati, A. Cerè, B. Chng, and C. Kurtsiefer, Reversing the Temporal Envelope of a Heralded Single Photon Using a Cavity, Phys. Rev. Lett. **113,** 163601 (2014).

[31] P. Farrera, G. Heinze, B. Albrecht, M. Ho, M. Chávez, C. Teo, N. Sangouard, and H. De Riedmatten, Generation of single photons with highly tunable wave shape from a cold atomic ensemble, Nat. Commun. **7,** 13556 (2016).

[32] D. E. Chang, A. S. Sørensen, P. R. Hemmer, and M. D. Lukin, Quantum Optics with Surface Plasmons, Phys. Rev. Lett. **97,** 053002 (2006).

[33] X.-W. Chen, V. Sandoghdar, and M. Agio, Highly efficient interfacing of guided plasmons and photons in nanowires, Nano Lett. **9,** 3756 (2009).

[34] C. Cohen-Tannoudji, J. Dupont-Roc, and G. Grynberg, *Atom-Photon Interactions: Basic Processes and Applications* (Wiley-VCH, New York, 1998).

[35] D. J. Moss, R. Morandotti, A. L. Gaeta, and M. Lipson, New cmos-compatible platforms based on silicon nitride and hydex for nonlinear optics, Nat. Photonics **7,** 597 (2013).

[36] X. Ji, F. A. S. Barbosa, S. P. Roberts, A. Dutt, J. Cardenas, Y. Okawachi, A. Bryant, A. L. Gaeta, and M. Lipson, Ultra-low-loss on-chip resonators with sub-milliwatt parametric oscillation threshold, Optica **4,** 619 (2017).

[37] H. Subbaraman, X. Xu, A. Hosseini, X. Zhang, Y. Zhang, D. Kwong, and R. T. Chen, Recent advances in silicon-based passive and active optical interconnects, Opt. Express **23,** 2487 (2015).

[38] T. S. Tsoi and C. K. Law, Single-photon scattering on Λ-type three-level atoms in a one-dimensional waveguide, Phys. Rev. A **80,** 033823 (2009).

[39] B. W. Shore, *Manipulating Quantum Structures Using Laser Pulses* (Cambridge University Press, Cambridge, 2011).

[40] E. Krune, K. Jamshidi, K. Voigt, L. Zimmermann, and K. Petermann, Jitter analysis of optical clock distribution networks in silicon photonics, J. Lightwave Technol. **32,** 4378 (2014).

[41] B. E. Little, S. T. Chu, H. A. Haus, J. Foresi, and J. Laine, Microring resonator channel dropping filters, J. Lightwave Technol. **15,** 998 (1997).

[42] M. Bahadori, M. Nikdast, S. Rumley, L. Y. Dai, N. Janosik, T. V. Vaerenbergh, A. Gazman, Q. Cheng, R. Polster, and K. Bergman, Design space exploration of microring resonators in silicon photonic interconnects: Impact of the ring curvature, J. Lightwave Technol. **36,** 2767 (2018).

[43] M. H. P. Pfeiffer, J. Liu, A. S. Raja, T. Morais, B. Ghadiani, and T. J. Kippenberg, Ultra-smooth silicon nitride

waveguides based on the damascene reflow process: Fabrication and loss origins, Optica **5**, 884 (2018).

[44] Z. Yao, K. Wu, B. X. Tan, J. Wang, Y. Li, Y. Zhang, and A. W. Poon, Integrated silicon photonic microresonators: Emerging technologies, IEEE J. Sel. Top. Quantum Electron. **24**, 1 (2018).

[45] D. K. Sparacin, C. yin Hong, L. C. Kimerling, J. Michel, J. P. Lock, and K. K. Gleason, Trimming of microring resonators by photo-oxidation of a plasma-polymerized organosilane cladding material, Opt. Lett. **30**, 2251 (2005).

[46] M.-C. M. Lee and M. C. Wu, Tunable coupling regimes of silicon microdisk resonators using mems actuators, Opt. Express **14**, 4703 (2006).

[47] T. Aoki, B. Dayan, E. Wilcut, W. P. Bowen, A. S. Parkins, T. J. Kippenberg, K. J. Vahala, and H. J. Kimble, Observation of strong coupling between one atom and a monolithic microresonator, Nature **443**, 671 (2006).

[48] M. De Feudis, A. Tallaire, L. Nicolas, O. Brinza, P. Goldner, G. Hétet, F. Bénédic, and J. Achard, Large-scale fabrication of highly emissive nanodiamonds by chemical vapor deposition with controlled doping by SiV and GeV centers from a solid source, Adv. Mater. Interfaces **7**, 1901408 (2020).

[49] H. Siampour, S. Kumar, V. A. Davydov, L. F. Kulikova, V. N. Agafonov, and S. I. Bozhevolnyi, On-chip excitation of single germanium vacancies in nanodiamonds embedded in plasmonic waveguides, Light Sci. Appl. **7**, 61 (2018).

[50] E. Janitz, M. K. Bhaskar, and L. Childress, Cavity quantum electrodynamics with color centers in diamond, Optica **7**, 1232 (2020).

[51] A. Schwagmann, S. Kalliakos, D. J. P. Ellis, I. Farrer, J. P. Griffiths, G. A. C. Jones, D. A. Ritchie, and A. J. Shields, In-plane single-photon emission from a L3 cavity coupled to a photonic crystal waveguide, Opt. Express **20**, 28614 (2012).

[52] S. Hepp, F. Hornung, S. Bauer, E. Hesselmeier, X. Yuan, M. Jetter, S. L. Portalupi, A. Rastelli, and P. Michler, Purcell-enhanced single-photon emission from a strain-tunable quantum dot in a cavity-waveguide device, Appl. Phys. Lett. **117**, 254002 (2020).

[53] J. W. Silverstone, D. Bonneau, J. L. O'Brien, and M. G. Thompson, Silicon quantum photonics, IEEE J. Sel. Top. Quantum Electron. **22**, 390 (2016).

[54] Y. Yin, Y. Chen, D. Sank, P. J. J. O'Malley, T. C. White, R. Barends, J. Kelly, E. Lucero, M. Mariantoni, A. Megrant, C. Neill, A. Vainsencher, J. Wenner, A. N. Korotkov, A. N. Cleland, and J. M. Martinis, Catch and Release of Microwave Photon States, Phys. Rev. Lett. **110**, 107001 (2013).

[55] P. Kurpiers, P. Magnard, T. Walter, B. Royer, M. Pechal, J. Heinsoo, Y. Salathé, A. Akin, S. Storz, J. C. Besse, S. Gasparinetti, A. Blais, and A. Wallraff, Deterministic quantum state transfer and remote entanglement using microwave photons, Nature **558**, 264 (2018).

[56] C. J. Axline, L. D. Burkhart, W. Pfaff, M. Zhang, K. Chou, P. Campagne-Ibarcq, P. Reinhold, L. Frunzio, S. M. Girvin, L. Jiang, M. H. Devoret, and R. J. Schoelkopf, On-demand quantum state transfer and entanglement between remote microwave cavity memories, Nat. Phys. **14**, 705 (2018).

[57] M. J. Weaver, F. Buters, F. Luna, H. Eerkens, K. Heeck, S. de Man, and D. Bouwmeester, Coherent optomechanical state transfer between disparate mechanical resonators, Nat. Commun. **8**, 824 (2017).

[58] M. Rezai, J. Wrachtrup, and I. Gerhardt, Coherence Properties of Molecular Single Photons for Quantum Networks, Phys. Rev. X **8**, 031026 (2018).

[59] X. Zhu, S. Saito, A. Kemp, K. Kakuyanagi, S.-I. Karimoto, H. Nakano, W. J. Munro, Y. Tokura, M. S. Everitt, K. Nemoto, M. Kasu, N. Mizuochi, and K. Semba, Coherent coupling of a superconducting flux qubit to an electron spin ensemble in diamond, Nature **478**, 221 (2011).

[60] M. Kervinen, I. Rissanen, and M. Sillanpää, Interfacing planar superconducting qubits with high overtone bulk acoustic phonons, Phys. Rev. B **97**, 205443 (2018).

[61] Y. Chu, P. Kharel, W. H. Renninger, L. D. Burkhart, L. Frunzio, P. T. Rakich, and R. J. Schoelkopf, Quantum acoustics with superconducting qubits, Science **358**, 199 (2017).

[62] M. O. Scully and M. S. Zubairy, *Quantum Optics* (Cambridge University Press, Cambridge, 1997).

[63] J.-T. Shen and S. Fan, Theory of single-photon transport in a single-mode waveguide. II. Coupling to a whispering-gallery resonator containing a two-level atom, Phys. Rev. A **79**, 023838 (2009).

[64] K. Srinivasan and O. Painter, Mode coupling and cavity–quantum-dot interactions in a fiber-coupled microdisk cavity, Phys. Rev. A **75**, 023814 (2007).

[65] Z. Liao, H. Nha, and M. S. Zubairy, Dynamical theory of single-photon transport in a one-dimensional waveguide coupled to identical and nonidentical emitters, Phys. Rev. A **94**, 053842 (2016).

[66] C. W. Gardiner and M. J. Collett, Input and output in damped quantum systems: Quantum stochastic differential equations and the master equation, Phys. Rev. A **31**, 3761 (1985).

[67] C. da Fonseca and J. Petronilho, Explicit inverses of some tridiagonal matrices, Linear Algebra Appl. **325**, 7 (2001).

[68] M. Hirsch, S. Smale, and R. Devaney, *Differential Equations, Dynamical Systems, and an Introduction to Chaos* (Elsevier Science, Amsterdam, 2012).